Measurement report: Can Zenith Wet Delay from GNSS "see" atmospheric turbulence? Insights from case studies across diverse climate zones

Gaël Kermarrec[1], Xavier Calbet[2], Zhiguo Deng[3], and Cintia Carbajal Henken[4]

[1]Institute for Meteorology und Climatology, Leibniz Universität Hannover, Herrenhäuser Str. 2, Hannover, Germany
[2]AEMET, C/ELeonardo Prieto Castro 8, Ciudad Universitaria, Madrid, Spain
[3]Deutsches GeoForschungsZentrum GFZ, Wissenschaftspark Albert Einstein, Telegrafenberg, Potsdam, Germany
[4]Institute of Meteorology, Freie Universität Berlin, Carl-Heinrich-Weg 6-10, Berlin, Germany

Correspondence: Gaël Kermarrec (kermarrec@meteo.uni-hannover.de)

Abstract.

Global Navigation Satellite Systems (GNSS) microwave signals are almost unaffected by clouds but are delayed as they travel the troposphere. The hydrostatic delay accounts for approximately 90% of the total delay and can be well modeled as a function of temperature, pressure, and humidity. On the other hand, the wet delay is highly

5 variable with space and time, making it difficult to model accurately. A zenith wet delay (ZWD) can be estimated as part of the GNSS positioning adjustment and is proportional to the specific humidity in the atmospheric boundary layer (ABL). Whereas its average term can describe mesoscale events, its small-scale component is associated with turbulent processes in the ABL and the focus of the present contribution. We introduce a new filtering and estimation strategy to analyze small-scale ZWD variations, addressing questions on daily or periodic variations of some

10 turbulent parameters, and the dependence of these parameters on climate zones. Five GNSS stations were selected for case studies, revealing promising specific daily and seasonal patterns depending on the estimated turbulence at the GNSS station (buoyancy or shear). This research lays the groundwork for more accurate models and prediction strategies for integrated WV turbulence. It has far-reaching applications, from nowcasting uncertainty assessments to the stochastic modeling for Very Large Baseline Interferometry or GNSS.

1 Introduction

15 The atmospheric boundary layer (ABL) spans from the Earth's surface to about 1-2 km above the ground. This layer experiences rapid atmospheric changes, including cloud formation and convective initiation, as well as intense precipitation events linked to elevated temperatures in the context of climate change (Webb et al., 2016). It is characterized by large sources of water vapor (WV).

20 Turbulent processes in the ABL trigger the redistribution of trace gases, aerosols, heat, WV, and momentum (Stull, 2003). Understanding the transport of such scalars is crucial across various fields, including meteorology,

hydrology (Shawon et al., 2021), agriculture (Curto et al., 2022), and air quality control (Zhou et al., 2022). More specifically, enhancing the characterization of WV content at small (turbulent) scales within the ABL will provide new insights, aiding in (i) the evaluation and improvement of turbulence parameterizations in numerical
25 weather prediction (NWP) models for nowcasting (Lee and Meyers, 2023), (ii) the refinement of Radiative Transfer Models (RTM, (Calbet et al., 2018)), which simulate the absorption and emission of atmospheric molecular constituents layer by layer, and (iii) the mitigation of atmospheric distortions in Interferometric Synthetic Aperture Radar (INSAR, Chang and He (2011)) or for Very Long Baseline Interferometry (VLBI, Teke et al. (2013)) and Global Navigation Satellite Systems (GNSS) stochastic description (Kermarrec and Schön, 2014).

30 Although microwave signals from high-rate GNSS are unaffected by clouds (Alshawaf et al., 2013), they still experience a tropospheric delay, which is estimated in the zenith direction during the positioning adjustment (Teunissen and Montenbruck, 2017). This delay is divided into two components: the dry delay and the zenith wet delay (ZWD), the latter being proportional to the specific humidity averaged vertically over the lower atmosphere (Bevis et al., 1992), and, thus, connected to WV content in the ABL. Like electromagnetic phase measurements
35 defined as the integrated refractivity index (Wheelon, 2001), ZWD can be decomposed into an average and a rapidly fluctuating term. This latter is related to atmospheric WV turbulence and is the topic of our contribution.

The spectral content or power spectral density (psd) of these temporal fluctuations is usually described by the von Kármán model (Wheelon, 2001). In its simplest form, this model consists of three parameters: (i) the slope or decay of psd at high frequencies (ii) a cutoff or transition frequency below which the spectrum saturates, and
40 (iii) a variance related to WV turbulence strength. All three quantities can be estimated conjointly with statistical methods. In the spatial domain and using the Taylor frozen hypothesis (Taylor, 1938), the cutoff is called the outer scale length. This parameter marks the end of the inertial range where isotropy can no longer be assumed (Basu and Holtslag, 2022), making it particularly intriguing. Improved characterization of the cutoff from ZWD will provide new insights into this region of the spectrum and improve the understanding of (integrated) WV
45 turbulence processes in the ABL. Before reaching ambitious goals such as uncertainty modeling in nowcasting, improved stochastic modeling of GNSS observations, or correction of satellite images from the retrieval of the turbulent parameters, the following simple yet challenging questions are to be addressed at first:

– Which methodology is suitable for filtering turbulent fluctuations and estimating the parameters (cutoff, turbulence strength)?

50 – Have the retrieved turbulent parameters daily or periodic variations, which would indicate that they can be used to characterize turbulence?

– Does the strength and cutoff estimated from ZWD fluctuations depend on the climate zone?

By answering these questions, we develop a solid methodology and pave the way for a more detailed study, up to deriving Machine Learning strategies to predict integrated WV turbulence in the zenith direction from GNSS

55   ZWD, see, e.g., Pierzyna et al. (2023) in the optical field for the refractivity index. In this first contribution, we will introduce a new filtering and estimation strategy to extract and analyze the small-scale variations from ZWD time series. We will show how cutoff and strength are related to each other through a high variety of case studies. To reach that goal, we have selected five GNSS stations worldwide which correspond to different climates or locations known for local effects such as gravity waves, wind shear, or the vicinity of the ocean. We will show that specific

60   daily and seasonal periodic patterns can be recognized, a first step toward deriving more accurate models and prediction strategies.

The remainder of this paper is as follows: in the first section, we will introduce the mathematical background to compute and filter the ZWD and retrieve the turbulent parameters. The second section presents results for the chosen GNSS stations located in different climate zones for two specific days (winter/summer). We conclude with

65   some general considerations and an outlook.

2   Mathematical background: ZWD and their fluctuations

In this section, we introduce how ZWD and ZWD fluctuations can be retrieved from GNSS observations and develop the methodology to estimate the turbulent parameters.

2.1   Estimation of ZWD

70   Atmospheric WV is responsible for the propagation delay experienced by GNSS signals, called the Slant Wet Delay and commonly defined as the integral of the wet refractivity along the slant path above the station (Bevis et al., 1992). Through GNSS positioning adjustment, the total atmospheric zenith delay (ZTD) can be estimated, which is decomposed into (i) a hydrostatic term and (ii) a term accounting for the wet delay called ZWD. The hydrostatic delay is effectively modeled using, for instance, the Saastamoninen approach (Saastamoinen, 1972) and is about

75   80–90% of the ZTD (Tregoning and Herring, 2006). The ZWD is proportional to the specific humidity q averaged in the vertical direction over the depth of the lower atmosphere H where WV is concentrated. It is expressed as

$$ZWD = \frac{1}{\kappa'} \int_0^H \rho q \, dz \tag{1}$$

with κ' a factor depending on the surface temperature and specific gas constant (Bevis et al., 1992).

2.2   ZWD fluctuations

80   Similar to atmospheric temperature, pressure, or wind (Wheelon, 2001), ZWD can be divided into two components expressed as

$$ZWD = \langle ZWD \rangle + ZWD' \tag{2}$$
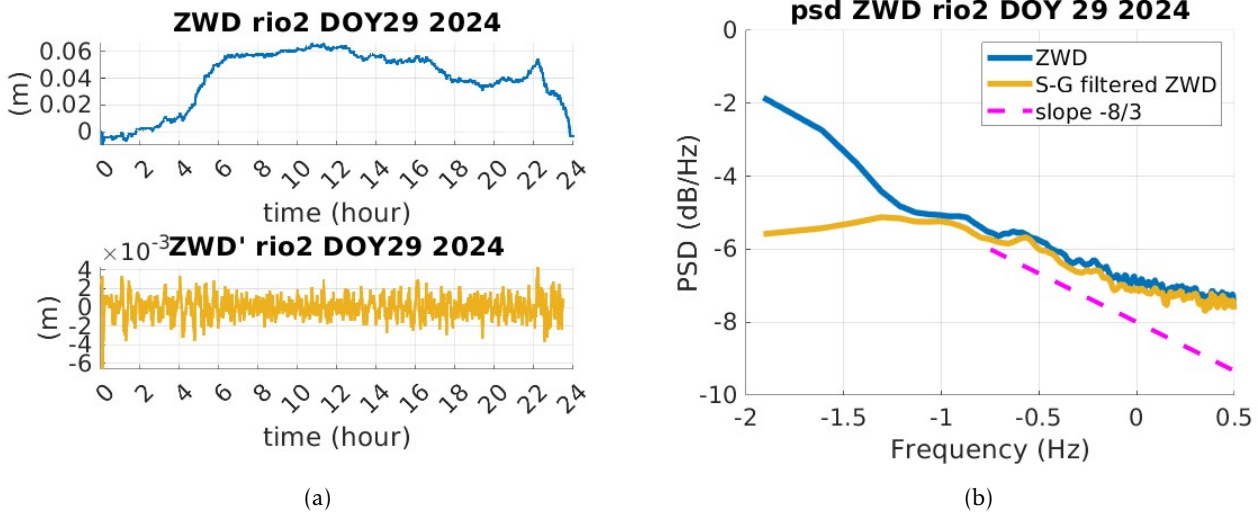
Figure 1. Illustration of the filtering of the ZWD from low-frequency effects related to mesoscale circulation. (a) top: the original ZWD, bottom: S-G filtered ZWD corresponding to $ZWD\prime$ and (b): the corresponding psd of GNSS station RIO2, DOY 29, 2024

where (i) $\langle ZWD \rangle$ describes mesoscale changes in the ambient value, such as gradual diurnal or seasonal variations, or sudden changes associated with weather fronts passing (Bevis et al., 1992), and (ii) $ZWD\prime$ is a random compo-

85 nent corresponding to turbulent fluctuations. This random component should be filtered from the estimated ZWD to enable a deeper study of its spectral content. Developing a proper methodology to achieve this goal is the central focus of this contribution.

2.2.1 Extracting the ZWD fluctuations

To study the ZWD fluctuations *only*, we filter $ZWD\prime$ from the ZWD time series using the Savitzky-Golay (S-G)

90 filter (Savitzky and Golay, 1964) with a Kaiser window weighting to limit boundary effects (Schmid et al., 2022). S-G filters are commonly used to "smooth out" noisy signals having a broad frequency range. Also known as digital smoothing polynomial filters or least-squares smoothing filters, the S-G filters often outperform standard averaging FIR filters by preserving high-frequency content - here the $ZWD\prime$ - and is the main reason why we have chosen this approach as in Kermarrec et al. (2023), besides its simplicity of use.

95 **Choice of the filter parameters**

The S-G filter uses a least-squares fit of a small set of consecutive data points to a polynomial. In each iteration, the central point of the fitted polynomial curve becomes the new smoothed data point. We assume that the integrated WV fluctuations in the ABL are stationary for about 30 minutes-1h so that the term $\langle ZWD \rangle$ should contain frequencies that are smaller than $1/3600 = 2.7e^{-4}$ Hz. These latter correspond to mesoscale effects and

100 should be filtered from the ZWD. To achieve the desired low-pass filtering effect at this specific cutoff frequency, two parameters must be adjusted: (i) the polynomial order d, typically set to 3 to prevent overfitting, and (ii)

the half-width of the smoothing window m. A large value of m will produce a very smoothed filtered time series $\langle ZWD \rangle$. Following Schafer (2011), we fix m based on the 3 dB cutoff frequency fc, which is given empirically by $fc = \frac{d+1}{3.2m-4.6}$. From physical considerations, the spectrum of $ZWD\prime$ is expected to saturate at a cutoff frequency

105   α between 0.1 and 0.005 Hz which corresponds approximately to an outer scale length of turbulence between 80 and 2000 m in the ABL assuming a geostropic wind velocity of $8ms^{-1}$ and the Taylor frozen hypothesis to hold, as described in Sect. 2.3 (Ziad, 2016). Thus, the S-G filter should remove frequencies slightly below α to ensure that *only* the low frequencies corresponding to $\langle ZWD \rangle$ are eliminated. We found the corresponding balance by setting $m = 300$ to select frequencies with a period slightly above 1 hour for observations at a data rate of 30 s. This way,

110   we can expect that the spectrum of $ZWD\prime$ will saturate and the mesoscale effects $\langle ZWD \rangle$ are eliminated. If this is not the case, implausibly small values of α will arise and be considered outliers, thus excluded from our analysis. Possible causes are related to the data themselves (outliers, small jumps, gaps) or turbulence effects (anisotropy, violation of the Kolmogorov assumption). A sensitivity analysis on m has shown that values varying m in the range of [220,350] did not affect the estimated parameters more than 5%, which is statistically negligible and will not

115   affect our conclusions.

The filter requires adjustment near sample boundaries when the window extends beyond the input vector. We use a Kaiser window to weight the time series as proposed in Schmid et al. (2022), with a value of 3 found optimal for ZWD.

Data processing and illustration of the filtering strategy

120   We estimate the ZTD from the GNSS observations of the stations described in Sect.3 using the Bernese GNSS Software (Dach et al., 2015) in Precise Point Positioning mode (Zumberge et al., 1997) at a 30-second rate. We do not constrain the ZTD to follow a random walk to avoid biasing the spectral content of the fluctuations term of the ZWD toward a specific power law (-2 from the random walk). We, thus, avoid obscuring the Kolmogorov turbulence spectrum (power law -8/3 corresponding to integrated water vapor, see Eq. 5 for more details). An

125   example of a ZWD for the station RIO2 on January 29, 2024, is provided in Fig. 1 (a), top. A significant increase in ZWD is noticeable around 4h, highlighting a specific mesoscale circulation for that day under consideration.

We illustrate the principle of the S-G filter by plotting the power spectral density (psd) before and after filtering in Fig. 1 (a) and (b). As shown in Fig. 1 (b) (yellow line), the low frequencies of ZWD (blue line) are eliminated properly, leading to a time series of fluctuations $ZWD\prime$ as shown in Fig. 1 (a) bottom. Its psd corresponds to a

130   van Kármán model (Sect. 2.2.2) with additional white noise, identified at high frequency. For visual analysis, the expected -8/3 slope is plotted as a magenta dotted line in Fig. 1 (b).

2.2.2 The spectrum of the ZWD fluctuations

Turbulent flow can be viewed as a collection of swirling motions called eddies or vortices. According to Kolmogorov, energy is transferred sequentially from larger to smaller eddies at a constant rate, a process known

135   as the turbulent energy cascade, which describes three-dimensional, isotropic, turbulence (Stull, 2003). The ABL

flows vary significantly based on the interaction between wind shear and buoyancy forces. Shear instabilities occur locally, while buoyancy forces create vigorous thermals that transport heat and momentum over larger distances. These forces can also work together to modify the flow dynamics within the ABL (Moeng and Sullivan, 1994).

In turbulence theory, the (spatial) power spectrum represents the distribution of kinetic energy of these eddies across various length scales. The inertial range of the spectrum corresponds to the length scales over which energy transfer occurs, with negligible dissipation due to molecular viscosity. The -5/3 power law of the energy spectrum can be derived from dimensional analysis and holds within the inertial range. In this region, Tatarski (Tatarski et al., 1961) proposed a Kolmogorov wave number spectrum (1D) for scalar quantities such as temperature or humidity as follows:

$$\Phi_x(k) = C_x k^{-5/3} \tag{3}$$

where Φ_x is the power spectrum of the scalar quantity x, k is the wave number, and C_x is a constant related to the structure of the turbulent field.

The von Kárman spectrum is mathematically more convenient as it avoids an infinite growth of the variance at large scales and is physically tractable (Wheelon, 2001). It is given in its simplest form by:

$$V_x(\kappa) \propto C_x^2 \left(\kappa^2 + \kappa_0^2\right)^{-5/6}, \tag{4}$$

and still has the typical -5/3 slope for the 1D case. The von Kárman spectrum saturates for small κ below the so-called outer scale length L_0 defined as $\kappa_0 = 2\pi/L_0$.

These formulas are valid for scalars such as humidity and temperature but have to be adapted for integrated scalars such as phase or ZWD. Since ZWD is a time series of integrated WV, we will now focus on deriving the temporal spectrum.

2.3 Taylor Frozen hypothesis

Despite the wind's stochastic nature over time and space, a temporal power spectrum can be derived from Eq. 4 under the Taylor frozen hypothesis (Taylor, 1938). This hypothesis assumes the medium remains static between measurements, with time translated into distance scaled by the velocity of turbulent irregularities.

Phase measurements of electromagnetic signals are proportional to the integrated refractivity index along the propagation path. The temporal power spectrum for the phase fluctuations can be derived using the van Kárman model and, per analogy, the power spectrum for integrated WV can be expressed as:

$$W_{intWV}(\omega) \propto \frac{C_{intWV}^2 v^{5/3}}{(\omega^2 + \kappa_0^2 v^2)^{5/6+1/2}} = \frac{C_{intWV}^2 v^{5/3}}{(\omega^2 + \kappa_0^2 v^2)^{4/3}}, \tag{5}$$

with v the wind velocity in the top part of the boundary layer (geostropic wind), C_{intWV}^2 the structure constant of the integrated WV, and $\kappa_0 = 2\pi v/L_0$. The spectrum exhibits a -8/3 slope and saturates at a cutoff frequency $\kappa_0 v$, see Wheelon (2001) or Ishimaru (2005) (in Appendix B).

The temporal spectrum W_{intWV} corresponds to a Matérn spectrum in statistics (Lilly et al., 2017) and can be parametrized in a simplified form as

$$W_x(\omega) = \frac{\sigma^2 \alpha^{5/3}}{c_\alpha(\omega^2 + \alpha^2)^\lambda}, \tag{6}$$

170   with $c_\alpha = \frac{1}{2/\pi} \frac{\Gamma(0.5)\Gamma(\lambda-0.5)}{\Gamma(\lambda)}$. This spectrum is described by three parameters: the variance σ^2, the slope λ, and α. The parametrization in Eq. 6 proves to be more convenient for numerical optimization during parameter fitting. The growth induced by turbulence is represented by the forcing parameter λ. To counteract this growth, a damping parameter called hereafter a "cutoff frequency" α is introduced. According to Kolmogorov theory, the slope is fixed at $\lambda = 4/3$ as in Eq. 5, leaving two parameters to estimate: α and σ^2, which is related to the strength of the WV
175   turbulence within the ABL.

2.4   Parameter estimation

The estimation of the two turbulence parameters mentioned in Sec. 2.3 from the empirical spectrum of observations often involves iterative regressions, as described in van Dinther and Hartogensis (2014). In this contribution, we propose an alternative method based on the theoretical understanding that the spectrum reflects a Matérn pro-
180   cess, as detailed in Eq. 6, see also Lilly et al. (2017) or Kermarrec and Schön (2020). The parameters α and σ can be estimated using a debiased version of the Weighted Maximum Likelihood Estimator (WMLE) (Sykulski et al., 2019). This method is highly effective for small sample sizes and, thus, advantageous given that stationarity for ZWD' should be maintained for only 30 minutes to 1 hour (equivalent to 120 samples at a 30 s data rate).

In this contribution, we have used an improved version of the algorithm to account for an additional white noise
185   by joint estimation (Montillet and Bos, 2020). We refer to Sykulski et al. (2019) for more details on the method. Because of the pre-filtering of the ZWD from mesoscale effects, the estimation of a random walk (slope of -2) is not mandatory which avoids a non-unique minimum in the estimation procedure.

As aforementioned, the cutoff frequency α and the variance of the process σ^2 are estimated by fixing the slope to $-8/3$ in the WMLE. We further constrain α between 0.005 and 0.1 Hz based on the physical considerations
190   mentioned in Sect. 2.3 given a wind velocity around $8 ms^{-1}$ (Ziad, 2016).

In Cheinet and Cumin (2011), temperature fluctuations (and similarly for the scalar WV) were shown to be log-normal distributed so that we can expect a normal distribution for the ZWD, which is favorable to the estimation strategy using MLE. We detect cases where our approach may fail (data gaps, outliers, non-stationarity, violation of the Taylor hypothesis) by computing the degree of error fit $error_{fit}$ between the natural log of the periodogram
195   and that of the fitted spectrum, more specifically the mean squared error between the two quantities. We filter such batches with a threshold-based outlier detection method for which values of $error_{fit}$ exceeding three standard deviations from the mean are excluded. Additionally, we ensure that α stays below 0.005 Hz from physical consideration and use a similar outlier detection on the contrary.

2.5 Summary of the methodology

200 Our methodology is summarized in Fig. 2 and in text form, as follows:

1. The processing of the GNSS raw observations using, e.g., the Bernese software, leads to the estimation of the ZWD.

2. The time series are filtered with the S-G filter to extract $ZWD\prime$ only.

3. The two parameters α and σ^2 are estimated batch-wise from the filtered $ZWD\prime$ time series. To that end, we
205   select a window of length LE corresponding to 1 hour of observations (LE=120 epochs for a data rate of 30s). In the second step, we let the window slide over the data and compute the parameters every 5 epochs (2.5 min for the given data rate). We obtain a time series of values from which we eliminate outliers by setting the lower limit to three standard deviations below the mean, and the upper limit to three standard deviations above the mean. Outliers are replaced by linear interpolation of neighboring, non-outlier values.

210 4. In the last step, the obtained time series of parameters α and σ^2 are smoothed using a moving average filter to ease interpretation and pattern recognition (periodicity, variations).
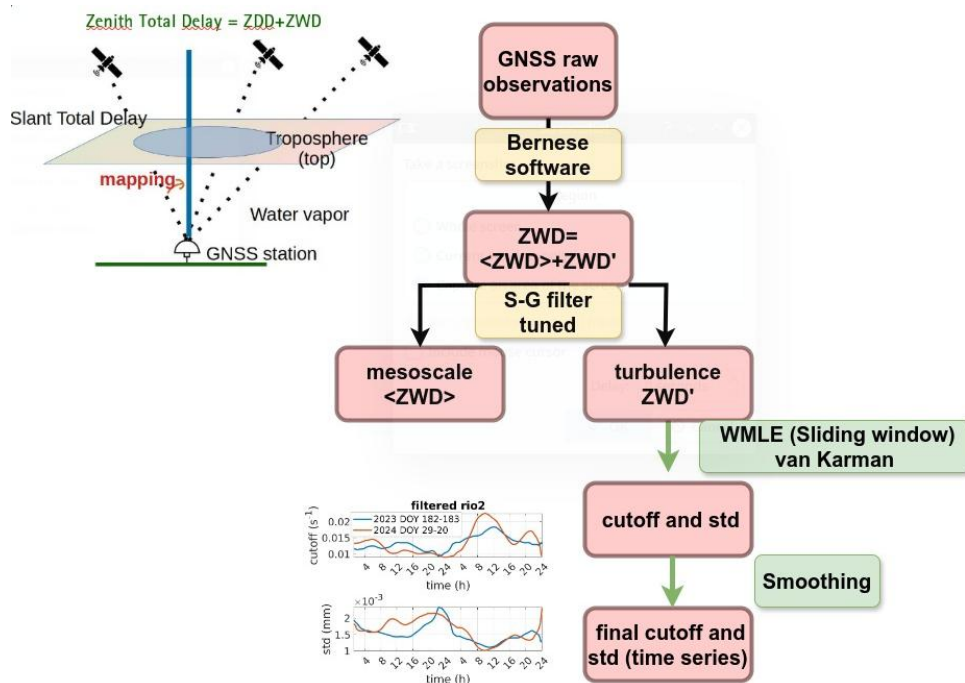
Figure 2. Flowchart summarizing the methodology from the processing of raw GNSS observations to the time series of turbulent parameters α et σ

3 Data and Results

3.1 GNSS observations

The time series of the 5 GNSS stations selected are located across the globe. To address the questions posed in the
215 introduction, we have chosen stations from the IGS located in different climate zones. At this stage, and for this
initial contribution to the topic, we aim to showcase the potential of our approach in offering new insights into at-
mospheric turbulence. The following stations were chosen as illustrated in Fig. 3, and the corresponding climates
are summarized in Tab 1. In the GNSS data processing we used the GeoForschungs Zentrum multi-GNSS satel-
lites orbit and clock product in Precise Point Positioning (PPP) mode. Thus, the error of satellites orbit and clock
220 can be ignored in this study. The 30-second ZWD are estimated in two steps: (i) Firstly, the GNSS data are pro-
cessed in PPP mode with standard parameter settings: ambiguities, 1-hour ZWD (with random-walk constrain),
24-hour station coordinates, 24-hour gradients and 30-second receiver clock error. Turbulence effects could be
partly absorbed by the estimated 30-second receiver clock parameters but the major part remains in the obser-
vation residuals. Outliers are removed using three times the interquartile range rule. After the first step, we get
225 clean GNSS observations and well-estimated parameters. In the second step, the estimated parameter corrections
(ambiguities, station coordinates, and gradients) from the first step are fixed. The 30-second ZWD and receiver
clock are, thus, estimated from the clean GNSS observations, their initial values being also from the first step. We
further mention that tropospheric effects were modeled using the VMF1 function (Boehm et al., 2006), IERS2010
conventions were applied to remove solid Earth and pole tides, and the FES2004 tidal model was used to model
230 ocean tide loading. Effects from, e.g., nontidal loading, multipath, or antenna center phase variations are expected
to be present in the residuals of the positioning adjustment and not in the ZWD, which is estimated as an indepen-
dent delay. Further, our strategy to analyze the turbulent parameters with the WMLE by fixing the slope should
eliminate such potential additional effects, if they were present in the ZWD.

Station	RIO2	URUM	UNB3	NYA2	SEY2
Climate	Gravity waves	Continental	Oceanic	Artic	Tropical

Table 1. Selected GNSS stations and their corresponding climates

For each station, we have selected two days of observations: one in winter (January 29, 2024, Date Of the Year
235 DOY 29) and one in summer (July 1, 2023, DOY 182), with winter and summer referring to the Northern Hemi-
sphere. We, thus, cover a broad range of turbulence situations by taking measurements from very different climate
zones and seasonal periods. While general conclusions or predictions with Machine Learning may require pro-
cessing more days of observations, the selected days already enable the identification of specific patterns. We have
further analyzed consecutive days that supported our conclusions. They are not shown for the sake of shortness
240 and readability in this contribution but are provided in the supplementary material (Kermarrec and Deng, 2024).
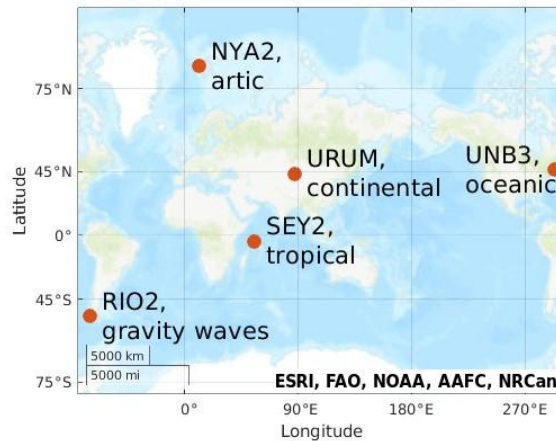
Figure 3. Worldmap illustrating the location of the selected IGS stations with the corresponding climate or specificity

We present the time series of ZWD, α and σ as well as the ratio $\frac{\sigma^2}{\alpha}$ for the two days under consideration. The ratio should help identify if the two estimated parameters have a linear dependency and have their minimum/maximum in phase. Such a dependency would ease prediction with Machine Learning as well as the establishment of local (i.e., station-related) models. WV turbulence may be affected by mesoscale effects so that ZWD plots are included

245   for completeness.

3.2 Climate zones

Continental climate: URUM

The station URUM is located in Urumqi (China). The city is situated in northwest China, near 44° North latitude, at an altitude ranging from 600 to 1000 m. The climate of Urumqi is arid continental, featuring freezing winters

250   and hot summers. The nearby mountains make precipitation more frequent in Urumqi than in other parts of the region, with generally light but frequent snowfalls in winter. In summer, occasional rain occurs, but dry periods can bring heat waves with highs reaching 38-40°C.

Figure 4 (a) top shows the ZWD for the two days under consideration (winter as a blue and summer as a red line, respectively). No strong variations are recorded except for the summer day where a local minimum can be

255   seen around 16h, with the decrease starting around 13h approximately. A similar decrease of the cutoff frequency α can be identified in Fig. 4 (b) top. The increase of σ^2 starts at a slower pace than α, as illustrated in Fig. 4 (a) bottom, with the time-dependent ratio σ^2/α (red line, positive slope). Interestingly, after the minimum around 16h, ZWD increases again but none of the turbulent parameters are affected by this change. It seems even that the drop in ZWD triggered an increase in the turbulence strength far after the minimum occurred. We note that α has

(a) (b)
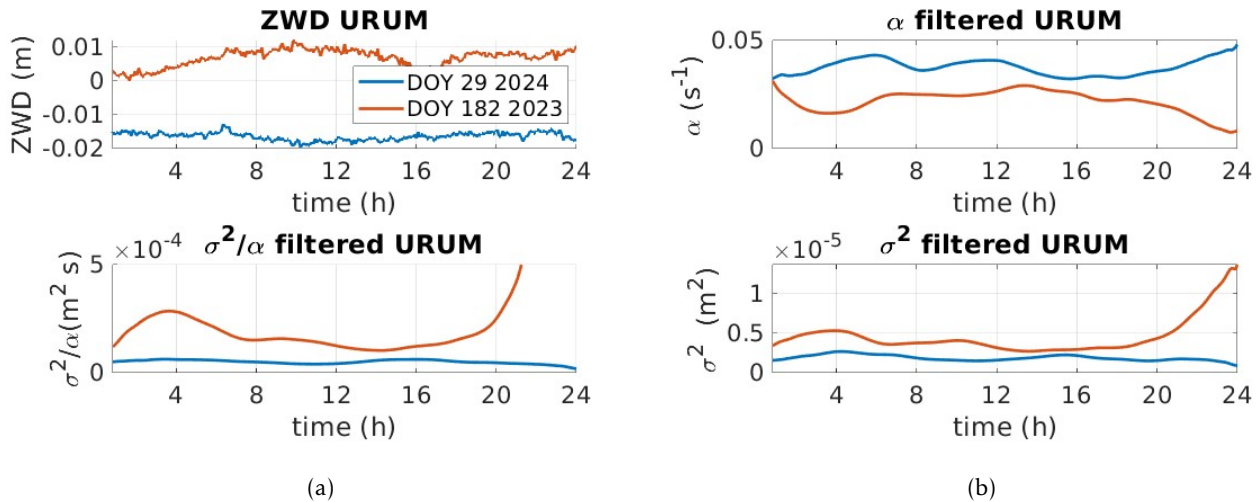
Figure 4. Station URUM (continental climate) (a) top: ZWD (m) for DOY 29, 2024 and DOY 182, 2023 and bottom: the ratio σ^2/α (b) top: the cutoff frequency α and bottom: the variance σ^2. For the sake of readability, we have subtracted 0.04 from the ZWD on DOY 29.

260 a minimum at 4h at night, corresponding to a maximum of σ^2. However, the ratio is not constant, thus does not allow deriving the proportionality relationship between the two parameters.

In winter, the turbulence strength σ^2 is smaller than in summer, and so is α correspondingly higher (blue line). The variations are less pronounced than in summer, making us think that the atmosphere may be more stratified and stable. Daily variations are not evident for the day under consideration and the ratio σ^2/α is nearly constant, 265 which is favorable for estimation.

3.3 Oceanic climate: UNB3

The IGS station UNB3 is one of several continuously operating GNSS reference stations in and near the Province of New Brunswick, Canada. It is located in the city of Fredericton. The receiver is part of SuomiNet which is a network of GNSS receivers at universities and other locations providing real-time atmospheric precipitable WV measure-270 ments and other geodetic and meteorological information. The station was used upon others in combination with GLONASS to monitor the ionosphere (Banville and Langley, 2015).

The climate at UNB3 is more coastal and maritime than in the inland of New Brunswick. Moist Atlantic air brings mild winter spells and cool summer periods.

From Fig. 5 (a) top, there is no evidence for strong changes in the WV content. A slow ZWD increase is visible 275 for the summer day starting around 8h, which can be put in parallel with a decrease of turbulence strength, see Fig. 5 (b) bottom (red line). The variations in α are similar although the variations are smaller than 0.01 Hz. This finding could be interpreted as the isotropic turbulence becoming less intense but the corresponding length of the
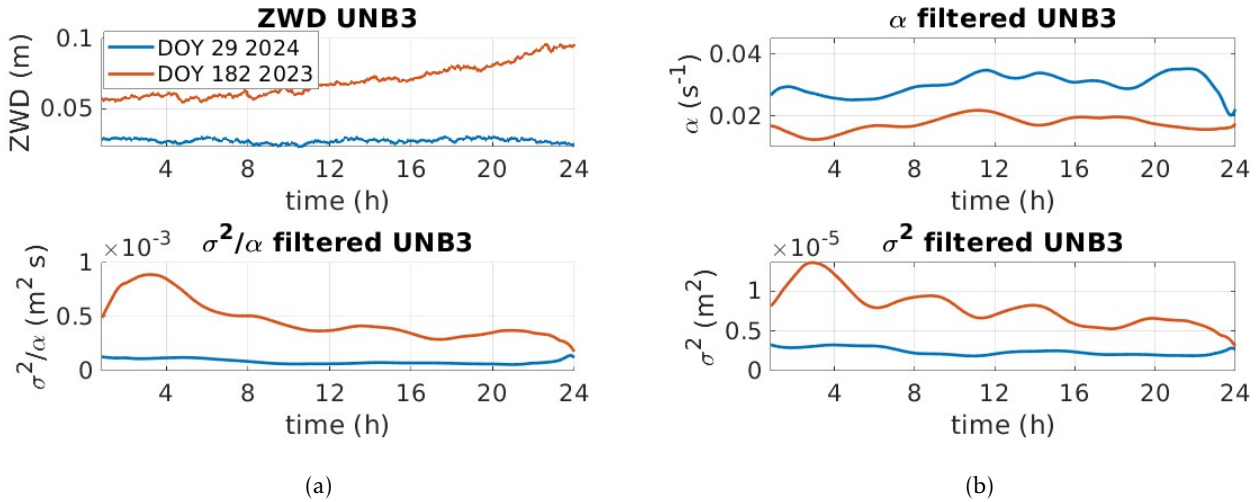
Figure 5. Station UNB3 (oceanic climate) (a) top: ZWD (m) for DOY 29, 2024 and DOY 182, 2023 and bottom: the ratio σ^2/α (b) top: the cutoff frequency α and bottom: the variance σ^2.

Kolmogorov bandwidth (inertial range) staying (nearly) constant over time (i.e., increasing less intensely than σ^2 decreases). This leads to a ratio σ^2/α which decreases linearly instead of remaining constant, so that no simple 280 proportionality constant can be deduced as for the winter case. A possible interpretation is that the integrated WV increase has damped isotropic turbulence to the profit of more elongated structures. We note an evident periodic variation of the turbulent parameters in summer, see Fig. 5 (b) with a period of around 4h. This pattern could be linked to specific daily mass movement but necessitates further investigations based on additional sensors.

In winter (blue line), on the contrary, the turbulent parameters are less variable. σ^2 indicates a less intense 285 turbulence strength than in summer. The periodic variations still exist but are less visible. The ratio σ^2/α is nearly constant with time, as for URUM.

Further, the mean value of α is smaller than for the continental case, which could be attributed to an increase in turbulence strength. In summer, σ^2 is more than 2 times higher than in winter for this day under consideration. σ^2 decreases during this particular day in summer so that the heating of the surface generating convective turbulence 290 cannot be made responsible for turbulence strength only. Additional investigations based on, e.g., the wind velocity would ease interpretation. The low value of α in summer let us think that the turbulence should be mostly isotropic (i.e., corresponding to a longer inertial range).

Arctic climate

Ny-Ålesund, located on a fjord on Svalbard's west coast, is influenced by warm ocean currents from lower lati-
295 tudes, affecting the local climate. Despite its high Arctic location (78.9°N, 11.9°E), summer temperatures remain above freezing, and winter temperatures rarely drop below -25°C, though they vary significantly from year to year (Maturilli et al., 2013). Männel et al. (2021) validated GNSS-based WV estimation with radiosonde data for 15
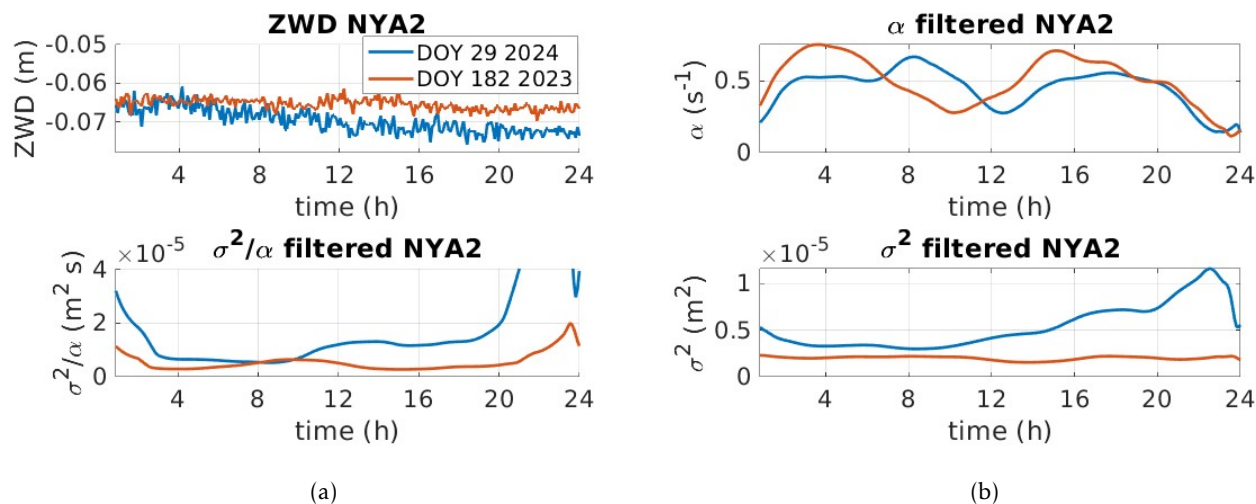
Figure 6. Station NYA2 (arctic climate) (a) top: ZWD (m) for DOY 29, 2024 and DOY 182, 2023 and bottom: the ratio σ^2/α (b) top: the cutoff frequency α and bottom: the variance σ^2. For the sake of readability, we have subtracted 0.1 from ZWD on DOY 182.

months of observations and could identify warm-air intrusion events. At mid-latitudes, the boundary layer is typically one or a few kilometers deep, but in the Arctic, it is much shallower, usually a few hundred meters or less.
300 This is due to the stable stratification caused by the increase in absolute temperature within the lowest kilometer (Mauritsen, 2007). Graßl et al. (2022) analyzed by high-resolution wind lidar data and found that the atmosphere from 400 m to 1000 m above Ny-Ålesund was characterized by a turbulent wind shear zone, linking the micrometeorology of the ABL with the synoptic flow.

From Fig. 6 (a) top, a slight decrease of ZWD is visible for the winter day (blue line) but no strong variations for
305 the summer day (red line). Interestingly, the decrease on DOY 29, 2024, is linked with an increase in the strength of turbulence σ^2, contrary to what we observed for the station UNB3 (Fig. 5 (b)). We further note that σ^2 is smaller in summer than in winter, which we could attribute to a more stable and stratified air. The values of α are similar for the two days under consideration but vary strongly during the day with an amplitude of more than 0.2Hz, see Fig. 6 (b) top. We identify an increase of α at night with a maximum at 4h and 16h in summer and a minimum at 10h and
310 midnight in winter. These maxima are delayed by about 2h in winter but still exhibit a period of approximately 4h. This finding could be linked with specific momentum (wind shear) above the station under consideration. We note that the ratio σ^2/α is not constant, particularly at night. However, in summer, its variations are small in comparison to winter. The high value of α combined with low values of σ^2 can be interpreted as a stratified and stable air, which is supported by the aforementioned studies.

315   The comparison between NYA2 and UNB3 shows that the turbulent parameters cannot be deduced by visual analysis of the ZWD; Their behavior cannot be predicted without a statistical estimation. Plausible explanations can be deduced from physical considerations depending on the climate or local conditions at the GNSS station.

RIA2: Tierra del fuego

Tierra del Fuego is located at the southern extremity of South America. The climate is consistently cooler in
320   summer and colder in winter, with significant contrasts in annual rainfall. This area is known as the world's gravity wave hotspot. Strong tropospheric winds create mountain waves year-round. In austral winter, the polar night jet's westerlies allow these waves to penetrate deep into the middle atmosphere, where they deposit momentum and slow the stratospheric flow (Kaifler et al., 2020). Gravity waves in the Earth's atmosphere play a crucial role in the geophysical system, facilitating the transfer of energy and momentum across different scales and connecting
325   various atmospheric layers (Wright et al., 2016). We further mention that RIA2 is located near the sea.

During the two days DOY 29, 2024, and 182, 2023, no strong gravity waves directly above the station could be visually identified at https://worldview.earthdata.nasa.gov/.

In Fig. 7 (a) top, a clear increase of ZWD is visible from 0 to 12h in winter (red line in that hemisphere). This increase is followed by a plateau from 13h when σ^2 starts its increase. Thus, the turbulence strength is triggered
330   by the variations but does not occur directly during the integrated WV increase. In winter, we note that σ^2 slightly increases during the day but stays at a low level (factor 10 lower than for the other stations under consideration, Fig. 7 (b) bottom, blue line). The parameter α is small which we will link with a very long inertial range and a rather isotropic and well-developed turbulence, most probably due to buoyancy. No strong difference can be identified between summer and winter, i.e., the blue and red curves follow each other. A periodic pattern can be identified
335   and the time between a maxima and a minima is around 2h thus much smaller than for the station NYA2. This finding supports our interpretation that a different type of turbulence occurs, potentially linked with air masses.

The ratio σ^2/α is nearly constant for the winter day, but increases during the day in summer making it difficult to find a proportionality constant, although a linear dependency with time could be deduced. More days of observations would be mandatory to deduce a general formula or for prediction.

340   We present in Appendix A the first results for a day with strong gravity waves. We show that the correspondence between the minimum of σ and the maximum of α does not seem to hold in that case, highlighting the impact of gravity waves on the low-frequency region of the spectrum. Such a behavior is promising yet necessitates deeper investigations, which is beyond the scope of this contribution.

SEY2: Tropical climate

345 We have selected the IGS station SEY2 located in the middle of the Seychelles island (height 580 m above the ellipsoid) to illustrate the tropical climate. Seychelles has a tropical climate with high humidity. Temperatures don't fluctuate much throughout the year. The island is surrounded by the Indian Ocean with no major land mass within a radius of at least 1600 km. This equatorial Indian Ocean is a key region for the initiation of the Madden-Julian Oscillation, which affects global weather and climate (Santosh, 2022). The lower troposphere and ABL near
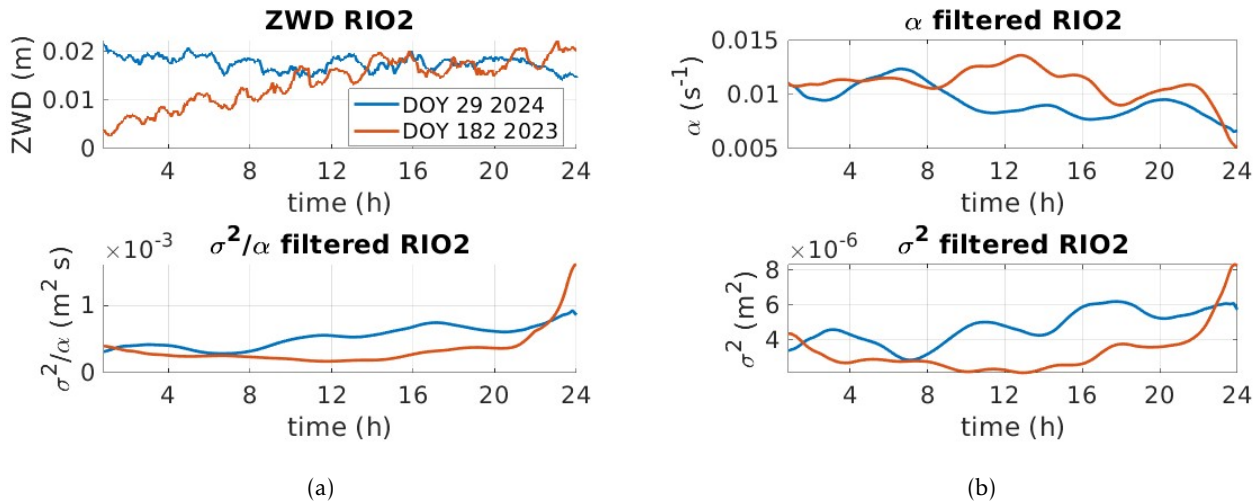
Figure 7. Station RIO2 (toundra, gravity waves) (a) top: ZWD (m) for DOY 29, 2024 and DOY 182, 2023 and bottom: the ratio σ^2/α (b) top: the cutoff frequency α and bottom: the variance σ^2.

350 Seychelles are crucial in the onset and eastward propagation of the MJO by regulating lower tropospheric moisture. Further, the ocean around Seychelles is part of the Seychelles–Chagos Thermocline Ridge, which may also play a significant role in the onset of the MJO (Yokoi et al., 2008). ZWD from GNSS observations could help understanding better the atmospheric processes in the Seychelles region, as systematic long-term data for the lower troposphere are still missing.

355 We can expect that a convective boundary layer forms over the small islands since marine air over small islands encounters a rougher, hotter surface than the ocean, creating a local hot spot. This may, however, not be the case for the SEY2 GNSS station located at the top of the mountain.

Indeed, for the two days DOY 29, 2024 and DOY 182, 2023, (summer and winter) no strong variations of the ZWD can be identified in Fig. 8 (a) top. However, for the selected days, we observe a decrease of σ^2 after 10h, linked

360 with an increase of α at the same time. This effect is stronger during winter (South hemisphere, red line) than in summer. It is most probably due to local atmospheric processes, maybe an increase of the convection at the sea level during the day. We note strong periodic variations (distance minima/maxima of 4h or less as for the other stations except UNB3). The minimum of σ^2 (maximum of α respectively) is delayed in winter compared to summer (14h versus 18h), an effect that could be physically explainable by, e.g., the time at which the maximum temperature is

365 reached (as the buoyancy would increase). Due to the location of the station, however, general conclusions should be made carefully.

The ratio σ^2/α is nearly constant before and after 10h and slightly higher for the winter day under consideration but hardly interpretable compared to the other stations. We found close results for two days in autumn and spring presented in Appendix B. The periodic variations in α for autumn (South hemisphere, DOY 099 2024) were strong

(a)   (b)
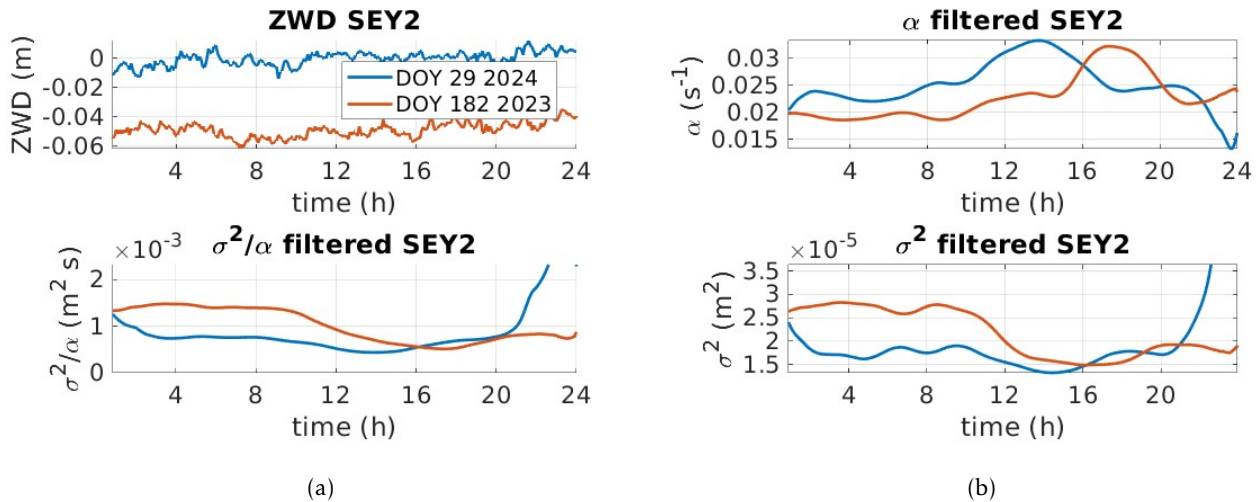
Figure 8. Station SEY2 (tropical climate) (a) top: ZWD (m) for DOY 29, 2024 and DOY 182, 2023 and bottom: the ratio σ^2/α (b) top: the cutoff frequency α and bottom: the variance σ^2.

370   with a period varying from 4h (afternoon) to 6h (morning) approximately. For spring (DOY 274 2023), the periodic variations were damped in the late afternoon. This could be linked with specific air masses movement creating buoyancy thus affecting the end of the inertial range (low frequency region).

4   Discussion and outlook

Enhancing the understanding of spatio-temporal characteristics of turbulent WV fluctuations will significantly
375   improve models for nowcasting extreme weather events. It will also shed light on turbulent processes in the energy input region, which remain only partially understood. Utilizing cost-effective, all-weather instruments like GNSS receivers, which offer the necessary accuracy, data rate, and spatial worldwide coverage, is a promising solution to reach that goal. This requires developing a reliable, statistically-based method for extracting relevant turbulence parameters from the estimated ZWD.
380   In this contribution, we have developed a new methodology to "extract" the turbulent fluctuations by filtering the ZWD from mesoscale effects. A S-G filter was tuned adequately to retrieve the part of the ZWD spectrum having a van Kármán spectrum content. We used a maximum likelihood approach to estimate the turbulent parameters: the cutoff frequency α corresponding to the end of the inertial range using the Taylor frozen hypothesis as well as the strength of turbulence σ^2 corresponding to the variance of the filtered (turbulent) process. To investigate the
385   extent to which those parameters may vary depending on the climate zone (or turbulence above the stations), on the time of the day or year (daily or seasonal pattern), we have selected randomly two days and 5 GNSS stations from the IGS network.

We could show that the variations of turbulence strength were related to the cutoff frequency in most cases, except for the station at the station RIO2 (Tierra del Fuego) for a day with strong gravity waves. This promising result
390 highlights the high potential of the analysis of the turbulent parameters to deepen our understanding of turbulent processes in the ABL related to WV fluctuations. A difference in winter/summer and day/night was visible for the oceanic and continental climate but not for the tropical climate. We could identify some dependencies between expected turbulence characteristics (buoyancy or wind shear) and the increase/decrease of σ^2 with respect to α. We identified a periodical pattern with a distance of 4h or less between maxima and minima, which could be related
395 to air masses and surface heating. This effect was slightly stronger during summer.

We point out that a joint interpretation (climate, location of the station) is mandatory for enhancing the global understanding of the time variations of turbulent parameters. The particular shapes found in our example make us confident that Machine Learning strategies could be used to identify the main dependencies and perform predictions. Our study is the first milestone in that direction using easily and worldwide available GNSS observations.
400 Validation strategies could include instruments such as eddy covariance (Sun et al., 2018) or Large Eddy Simulations (Maronga et al., 2020). We found promising dependencies using a gradient boosting algorithm, as in Pierzyna et al. (2024) with the vertical wind velocity and the Total Kinetic Energy retrieved from lidar measurements at 1500 m height using GNSS observations from the station PAYN in Switzerland. The corresponding results will be summarized in our next contribution.

405 **Appendix A: RIO2: gravity waves**

In this Appendix, we show the potential impact of gravity on the cutoff frequency α. To reach that goal, we have selected at https://worldview.earthdata.nasa.gov/ one day at which gravity waves above RIO2 (located as shown in http://geodesy.unr.edu/NGLStationPages/stations/RIO2.sta) could be visually identified from the corrected reflectance (DOY 135, 2024). The Visible Infrared Imaging Radiometer Suite (VIIRS) Corrected Reflectance imagery
410 is available in near real-time from the Suomi NPP satellite, operated by NASA and NOAA. This imagery has a daily sensor resolution of 750 m and 375. For comparison, we also computed the days DOY 135 and 136, red and yellow lines respectively in Fig, A1). The ZWD for the three days under consideration do not exhibit strong variations, i.e. a light continuous increase for DOY 135 and 136 only. The values for σ^2 highlight an increase of turbulence in the evening from 16-20h and a periodic pattern as in Fig. 7. On DOY 169, σ^2 is nearly constant with a strong
415 sinus-like shape. This latter is also visible in α with a nice correspondence between the minima and maxima of the two quantities. A similar behavior is visible for DOY 135 (yellow line). However, on DOY 134 (blue line), it is evident that the strong maximum of α around 13h is not linked with a minimum of σ^2 as usual. We are intended to think that this behavior could be due to the gravity waves: These latter would affect the low frequency region of the spectrum associated with large scales, without impacting the strength of turbulence. This remains to be confirmed
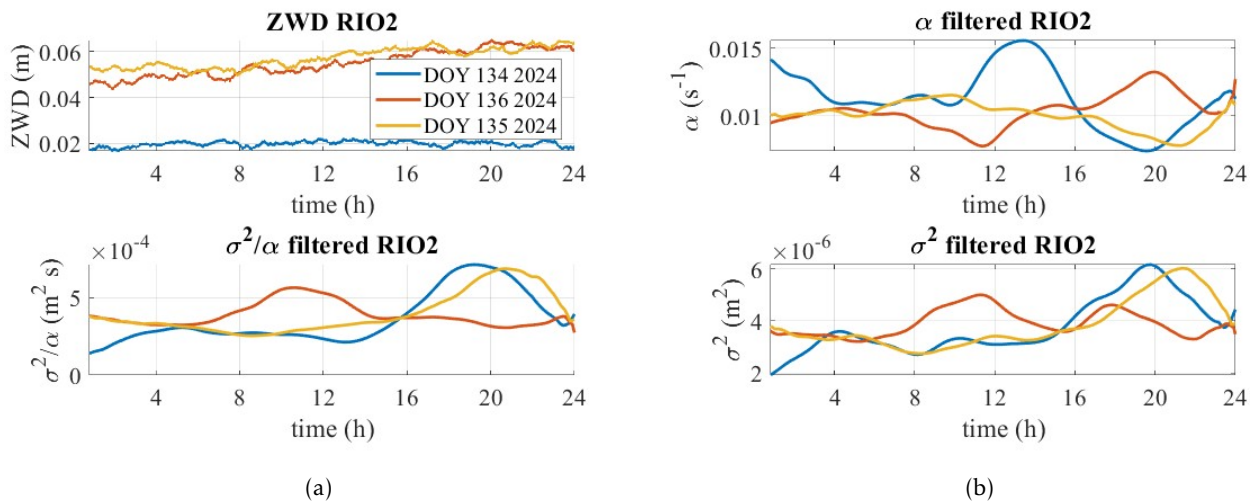
Figure A1. Station RIO2 (gravity waves) (a) top: ZWD (m) for DOY 134, 2024, DOY 135, 2024 and DOY 136, 2024. bottom: the ratio σ^2/α (b) top: the cutoff frequency α and bottom: the variance σ^2.

420   in a next contribution but highlights already the high potential of ZWD to study specific atmospheric effects in the ABL related to turbulence.

<table>
<tr><td>(a)</td><td>(b)</td></tr>
</table>
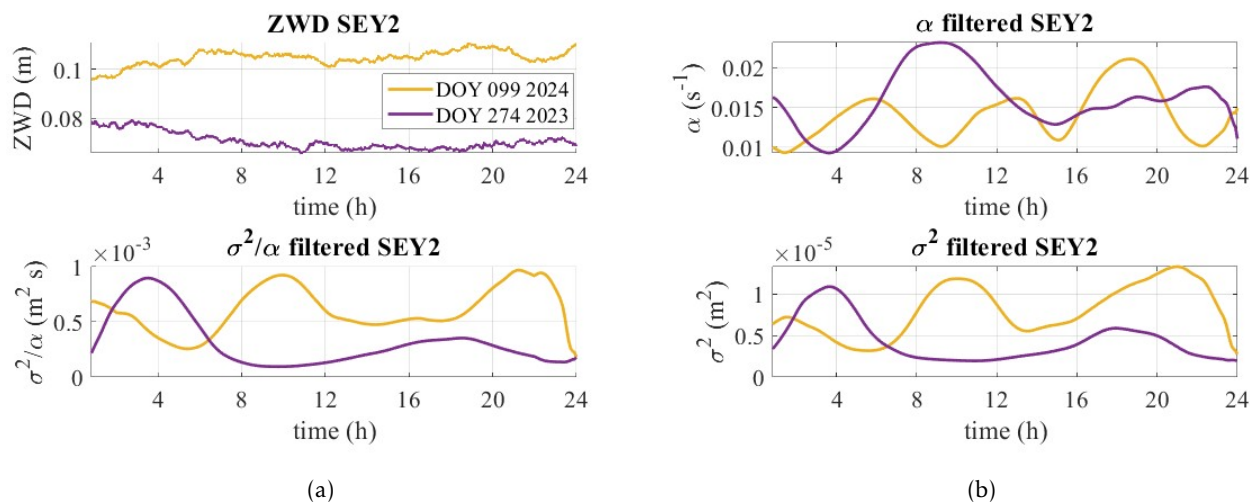
Figure B1. Station SEY2 (tropical climate) (a) top: ZWD (m) for DOY 099, 2024, DOY 273, 2023. bottom: the ratio σ^2/α (b) top: the cutoff frequency α and bottom: the variance σ^2.

Appendix B: SEY2: automn and spring

For the sake of completeness and because the spring and autumn seasons may be slightly different than summer and winter for the tropical climate, we have added two days DOY 099, 2024 and DOY 274,2023 presented in

425 Fig. B1. The description and analysis are provided in the main body.

Author contributions. G.Kermarrec developed the methodology and performed the estimation of the turbulence parameter estimation as well as their analysis. She wrote the manuscript. Z.Deng made the ZWD computation at the GfZ, Potsdam, Germany. X.Calbet discussed the results from a meteorological perspective. He and C.Carbajal Henken provided guidance and reviewed the original manuscript.

430 *Competing interests.* The authors declare no conflict of interest

Acknowledgements. This study is supported by the Deutsche Forschungsgemeinschaft under the project KE2453/2-1 for correlation analysis within the context of optimal fitting.

Code and data availability. For the computation of the turbulent parameters, we made use of the software jLab v1.7.2 by J. M. Lilly "A data analysis toolbox for Matlab, including routines for big data analysis, signal processing, mapping, and oceano-
435 graphic applications." retrieved at https://www.jmlilly.net/doc/jLab.html. All time series used in this article are available publicly at Kermarrec and Deng (2024)

, DOI https://doi.org/10.25835/HCC01FRE

References

Alshawaf, F., Fuhrmann, T., Heck, B., Hinz, S., Knöpfler, A., Luo, X., Mayer, M., Schenk, A., Thiele, A., and Westerhaus, M.:
440   Integration of InSAR and GNSS Observations for the Determination of Atmospheric Water Vapour, pp. 147–162, Springer
        Berlin Heidelberg, Berlin, Heidelberg, ISBN 978-3-642-32714-8, https://doi.org/10.1007/978-3-642-32714-8_10, 2013.

Banville, S. and Langley, R. B.: Monitoring the Ionosphere Using Integer-Leveled GLONASS Measurements, in: Proceedings
        of the 28th International Technical Meeting of the Satellite Division of The Institute of Navigation (ION GNSS+ 2015), pp.
        3578–3588, Tampa, Florida, 2015.

445 Basu, S. and Holtslag, A.: Revisiting and revising Tatarskii's formulation for the temperature structure parameter (χ_T) in atmo-
        spheric flows, Environ Fluid Mech, 22, 1107–1119, https://doi.org/10.1007/s10652-022-09880-3, 2022.

Bevis, M., Businger, S., Herring, T. A., Rocken, C., Anthes, R. A., and Ware, R. H.: GPS Meteorology: Remote Sensing of Atmo-
        spheric Water Vapor Using the Global Positioning System, Journal of Geophysical Research, 97, 15 787–15 801, 1992.

Boehm, J., Werl, B., and Schuh, H.: Troposphere mapping functions for GPS and very long baseline interferometry from
450   European Centre for Medium-Range Weather Forecasts operational analysis data, Journal of Geophysical Research, 111,
        https://doi.org/10.1029/2005JB003629, 2006.

Calbet, X., Peinado-Galan, N., DeSouza-Machado, S., Kursinski, E. R., Oria, P., Ward, D., Otarola, A., Rípodas, P., and Kivi,
        R.: Can turbulence within the field of view cause significant biases in radiative transfer modeling at the 183 GHz band?,
        Atmospheric Measurement Techniques, 11, 6409–6417, https://doi.org/10.5194/amt-11-6409-2018, 2018.

455 Chang, L. and He, X.: InSAR atmospheric distortions mitigation: GPS observations and NCEP FNL data, Journal of Atmospheric
        and Solar-Terrestrial Physics, 73, 464–471, https://doi.org/https://doi.org/10.1016/j.jastp.2010.11.003, 2011.

Cheinet, S. and Cumin, P.: Local Structure Parameters of Temperature and Humidity in the Entrainment-Drying Convective
        Boundary Layer: A Large-Eddy Simulation Analysis, Journal of Applied Meteorology and Climatology, 50, 472–481, http:
        //www.jstor.org/stable/26174035, 2011.

460 Curto, L., Gassmann, M. I., Covi, M., and Tonti, N. E.: Study of turbulence behavior above two different crops, Agricultural and
        Forest Meteorology, 322, 109 012, https://doi.org/https://doi.org/10.1016/j.agrformet.2022.109012, 2022.

Dach, R., Andritsch, F., Arnold, D., Bertone, S., Fridez, P., Jäggi, A., Jean, Y., Maier, A., Mervart, L., Meyer, U., Orliac, E.,
        Geist, E., Prange, L., Scaramuzza, S., Schaer, S., Sidorov, D., Susnik, A., Villiger, A., Walser, P., and Thaller, D.: Bernese
        GNSS Software Version 5.2, Astronomical Institute, University of Bern, Bern Open Publishing, ISBN 978-3-906813-05-9,
465   https://doi.org/10.7892/boris.72297, 2015.

Graßl, S., Ritter, C., and Schulz, A.: The Nature of the Ny-Ålesund Wind Field Analysed by High-Resolution Wind Lidar Data,
        Remote Sensing, 14, https://doi.org/10.3390/rs14153771, 2022.

Ishimaru, A.: Wave propagation and scattering in Random Media, IEEE Press, 2005.

Kaifler, N., Kaifler, B., and Dörnbrack, A. e. a.: Lidar observations of large-amplitude mountain waves in the stratosphere above
470   Tierra del Fuego, Argentina, Sci Rep, 10, 14 529, https://doi.org/10.1038/s41598-020-71443-7, 2020.

Kermarrec, G. and Deng, Z.: Zenithwetdelay, https://doi.org/10.25835/HCC01FRE, 2024.

Kermarrec, G. and Schön, S.: On the Mátern covariance family: a proposal for modeling temporal correlations based on turbu-
        lence theory, Journal of Geodesy, 88, 1061–1079, 2014.

Kermarrec, G. and Schön, S.: On the determination of the atmospheric outer scale length of turbulence using GPS phase differ-ence observations: the Seewinkel network, Earth, Planets and Space, 72, 1–16, 2020.

Kermarrec, G., Klos, A., Lenczuk, A., and Bogusz, J.: Long-term temporal-scales of hydrosphere changes observed by GPS over Europe: a comparison with GRACE and ENSO, IEEE Geoscience and Remote Sensing Letters, PP, 1–1, https://doi.org/10.1109/LGRS.2023.3345540, 2023.

Lee, T. R. and Meyers, T. P.: New Parameterizations of Turbulence Statistics for the Atmospheric Surface Layer, Monthly Weather Review, 151, 85 – 103, https://doi.org/10.1175/MWR-D-22-0071.1, 2023.

Lilly, J. M., Sykulski, A. M., Early, J. J., and Olhede, S. C.: Fractional Brownian motion, the Matérn process, and stochastic modeling of turbulent dispersion, Nonlinear Processes in Geophysics, 24, 481–514, https://doi.org/10.5194/npg-24-481-2017, 2017.

Männel, B., Zus, F., Dick, G., Glaser, S., Semmling, M., Balidakis, K., Wickert, J., Maturilli, M., Dahlke, S., and Schuh, H.: GNSS-based water vapor estimation and validation during the MOSAiC expedition, Atmospheric Measurement Techniques, 14, 5127–5138, https://doi.org/10.5194/amt-14-5127-2021, 2021.

Maronga, B., Banzhaf, S., Burmeister, C., Esch, T., Forkel, R., Fröhlich, D., Fuka, V., Gehrke, K. F., Geletič, J., Giersch, S., Grone-meier, T., Groß, G., Heldens, W., Hellsten, A., Hoffmann, F., Inagaki, A., Kadasch, E., Kanani-Sühring, F., Ketelsen, K., Khan, B. A., Knigge, C., Knoop, H., Krč, P., Kurppa, M., Maamari, H., Matzarakis, A., Mauder, M., Pallasch, M., Pavlik, D., Pfafferott, J., Resler, J., Rissmann, S., Russo, E., Salim, M., Schrempf, M., Schwenkel, J., Seckmeyer, G., Schubert, S., Sühring, M., von Tils, R., Vollmer, L., Ward, S., Witha, B., Wurps, H., Zeidler, J., and Raasch, S.: Overview of the PALM model system 6.0, Geoscientific Model Development, 13, 1335–1372, https://doi.org/10.5194/gmd-13-1335-2020, 2020.

Maturilli, M., Herber, A., and König-Langlo, G.: Climatology and time series of surface meteorology in Ny-Ålesund, Svalbard, Earth System Science Data, 5, 155–163, https://doi.org/10.5194/essd-5-155-2013, 2013.

Mauritsen, T.: On the Arctic Boundary Layer: From Turbulence to Climate, Ph.D. thesis, Meteorologiska institutionen (MISU), phD dissertation, 2007.

Moeng, C.-H. and Sullivan, P. P.: A Comparison of Shear- and Buoyancy-Driven Planetary Boundary Layer Flows, Journal of Atmospheric Sciences, 51, 999 – 1022, https://doi.org/10.1175/1520-0469(1994)051<0999:ACOSAB>2.0.CO;2, 1994.

Montillet, J. P. and Bos, M. S.: Geodetic Time Series Analysis in Earth Sciences, Geodetic Time Series Analysis in Earth Sciences, 2020.

Pierzyna, M., Saathof, R., and Basu, S.: Π-ML: A Dimensional Analysis-Based Machine Learning Parameterization of Optical Turbulence in the Atmospheric Surface Layer, Opt. Lett., 48, 4484–4487, https://doi.org/10.1364/OL.492652, 2023.

Pierzyna, M., Basu, S., and Saathof, R.: OTCliM: generating a near-surface climatology of optical turbulence strength (C_n^2) using gradient boosting, https://arxiv.org/abs/2408.00520, 2024.

Saastamoinen, J.: Contributions to the theory of atmospheric refraction, Bulletin Géodésique (1946-1975), 105, 279–298, 1972.

Santosh, M.: Structure and development of the atmospheric boundary layer over a small island (Mahé Island, Seychelles) in the equatorial Indian Ocean, Meteorology and Atmospheric Physics, 134, 91, https://doi.org/10.1007/s00703-022-00924-3, 2022.

Savitzky, A. and Golay, M. J. E.: Smoothing and Differentiation of Data by Simplified Least Squares Procedures., Analytical Chemistry, 36, 1627–1639, https://doi.org/10.1021/ac60214a047, 1964.

Schafer, R. W.: On the frequency-domain properties of Savitzky-Golay filters, in: 2011 Digital Signal Processing and Signal Processing Education Meeting (DSP/SPE), pp. 54–59, https://doi.org/10.1109/DSP-SPE.2011.5739186, 2011.

Schmid, M., Rath, D., and Diebold, U.: Why and How Savitzky–Golay Filters Should Be Replaced, ACS Measurement Science Au, 2, 185–196, https://doi.org/10.1021/acsmeasuresciau.1c00054, 2022.

Shawon, A. S. M., Prabhakaran, P., Kinney, G., Shaw, R. A., and Cantrell, W.: Dependence of aerosol-droplet partitioning on turbulence in a laboratory cloud, Journal of Geophysical Research: Atmospheres, 126, e2020JD033 799, https://doi.org/10.1029/2020JD033799, 2021.

Stull, R. B.: An introduction to boundary layer meteorology, Kluwer Academic Publishers, 2003.

Sun, J., Hu, W., Wang, N., et al.: Eddy covariance measurements of water vapor and energy flux over a lake in the Badain Jaran Desert, China, Journal of Arid Land, 10, 517–533, https://doi.org/10.1007/s40333-018-0057-3, 2018.

Sykulski, A. M., Olhede, S. C., Guillaumin, A. P., Lilly, J. M., and Early, J. J.: The debiased Whittle likelihood, Biometrika, 106, 251–266, 2019.

Tatarski, V. I., Silverman, R. A., and Chako, N.: Wave Propagation in a Turbulent Medium, 1961.

Taylor, G. I.: The Spectrum of Turbulence, Proceedings of the Royal Society of London. Series A - Mathematical and Physical Sciences, 164, 476–490, https://doi.org/10.1098/rspa.1938.0032, 1938.

Teke, K., Nilsson, T., Böhm, J., Hobiger, T., Steigenberger, P., García-Espada, S., Haas, R., and Willis, P.: Troposphere delays from space geodetic techniques, water vapor radiometers, and numerical weather models over a series of continuous VLBI campaigns, Journal of Geodesy, 87, 981–1001, 2013.

Teunissen, P. and Montenbruck, O.: Springer Handbook of Global Navigation Satellite Systems, Springer International Publishing, 2017.

Tregoning, P. and Herring, T. A.: Impact of a priori zenith hydrostatic delay errors on GPS estimates of station heights and zenith total delays, Geophysical Research Letters, 33, 2006.

van Dinther, D. and Hartogensis, O. K.: Using the Time-Lag Correlation Function of Dual-Aperture Scintillometer Measurements to Obtain the Crosswind, Journal of Atmospheric and Oceanic Technology, 31, 62 – 78, https://doi.org/10.1175/JTECH-D-13-00118.1, 2014.

Webb, S. R., Penna, N. T., Clarke, P. J., Webster, S., Martin, I., and Bennitt, G. V.: Kinematic GNSS Estimation of Zenith Wet Delay over a Range of Altitudes, Journal of Atmospheric and Oceanic Technology, 33, 3 – 15, https://doi.org/10.1175/JTECH-D-14-00111.1, 2016.

Wheelon, A. D.: Electromagnetic scintillation, Cambridge University Press, 2001.

Wright, C. J., Hindley, N. P., Moss, A. C., and Mitchell, N. J.: Multi-instrument gravity-wave measurements over Tierra del Fuego and the Drake Passage – Part 1: Potential energies and vertical wavelengths from AIRS, COSMIC, HIRDLS, MLS-Aura, SAAMER, SABER and radiosondes, Atmospheric Measurement Techniques, 9, 877–908, https://doi.org/10.5194/amt-9-877-2016, 2016.

Yokoi, T., Tozuka, T., and Yamagata, T.: Seasonal variation of the Seychelles Dome, Journal of Climate, 21, 3740–3754, https://doi.org/10.1175/2008JCLI1957.1, 2008.

Zhou, Y., Guo, J., Zhao, T., Lv, J., Bai, Y., Wang, C., et al.: Roles of atmospheric turbulence and stratification in a regional pollution transport event in the middle reaches of the Yangtze River, Earth and Space Science, 9, e2021EA002 062, https://doi.org/10.1029/2021EA002062, 2022.

Ziad, A.: Review of the Outer Scale of the Atmospheric Turbulence, in: Adaptive Optics Systems V, vol. 9909, p. 99091K, SPIE,
550   https://doi.org/10.1117/12.2231375, 2016.

Zumberge, J., Heflin, M., Jefferson, D., Watkins, M., and Webb, F.: Precise point positioning for the efficient and robust analysis
      of GPS data from large networks, Journal of Geophysical Research, 102, 1997.